



# The spatial distribution of water in the inner coma of Comet 9P/Tempel 1: Comparison between models and observations



S. Finklenburg<sup>a,\*</sup>, N. Thomas<sup>a</sup>, C.C. Su<sup>b</sup>, J.-S. Wu<sup>b</sup>

<sup>a</sup> Physikalisches Institut, University of Bern, Sidlerstrasse 5, CH-3012 Bern, Switzerland

<sup>b</sup> Department of Mechanical Engineering, National Chiao Tung University, 1001 Ta-Hsueh Road, Hsinchu 30010, Taiwan

## ARTICLE INFO

### Article history:

Received 14 November 2013

Revised 6 March 2014

Accepted 24 March 2014

Available online 2 April 2014

### Keywords:

Comet Tempel 1

Comets, coma

Comets, nucleus

## ABSTRACT

The near nucleus coma of Comet 9P/Tempel 1 has been simulated with the 3D Direct Simulation Monte Carlo (DSMC) code PDSC<sup>++</sup> (Su, C.-C. [2013]. Parallel Direct Simulation Monte Carlo (DSMC) Methods for Modeling Rarefied Gas Dynamics. PhD Thesis, National Chiao Tung University, Taiwan) and the derived column densities have been compared to observations of the water vapour distribution found by using infrared imaging spectrometer on the Deep Impact spacecraft (Feaga, L.M., A'Hearn, M.F., Sunshine, J.M., Groussin, O., Farnham, T.L. [2007]. *Icarus* 191(2), 134–145. <http://dx.doi.org/10.1016/j.icarus.2007.04.038>). Modelled total production rates are also compared to various observations made at the time of the Deep Impact encounter. Three different models were tested. For all models, the shape model constructed from the Deep Impact observations by Thomas et al. (Thomas, P.C., Veverka, J., Belton, M.J.S., Hidy, A., A'Hearn, M.F., Farnham, T.L., et al. [2007]. *Icarus*, 187(1), 4–15. <http://dx.doi.org/10.1016/j.icarus.2006.12.013>) was used. Outgassing depending only on the cosine of the solar insolation angle on each shape model facet is shown to provide an unsatisfactory model. Models constructed on the basis of active areas suggested by Kossacki and Szutowicz (Kossacki, K., Szutowicz, S. [2008]. *Icarus*, 195(2), 705–724. <http://dx.doi.org/10.1016/j.icarus.2007.12.014>) are shown to be superior. The Kossacki and Szutowicz model, however, also shows deficits which we have sought to improve upon. For the best model we investigate the properties of the outflow.

© 2014 Elsevier Inc. All rights reserved.

## 1. Introduction

### 1.1. General introduction

Comet 9P/Tempel 1 was discovered in 1867 and is a Jupiter-family comet with an orbital period of 5.5 years and a perihelion distance of 1.51 AU. It was encountered by the Deep Impact spacecraft on 2005 July 4, one day before perihelion. The peak outgassing currently occurs before perihelion and the water production rate is then about  $5\text{--}10 \times 10^{27}$  molecules per second (A'Hearn and Combi, 2007). The thermal inertia was found to be very low (Groussin et al., 2007a, 2007b). Sunshine et al. (2006) discovered water ice patches on the surface but they were too small and too few to explain the total water production rate. These results imply gas emission from ice just below the visible surface or from a surface layer dominated by dark material intimately mixed with the ice.

Tempel 1 is the first comet for which there is a detailed shape model (Thomas et al., 2007, 2013) as well as observations of the

gas distribution in the innermost coma (Feaga et al., 2007). This allows one to study the importance of the surface shape for the gas distribution and make detailed comparisons between model results and observations. Crifo et al. (2002) suggested that many of the observed features in the near nucleus coma of comets can be explained by an irregular shape. They suggested that, in the case of Comet 1P/Halley, the main structure of the coma could be simulated by low order spherical harmonics of the shape. This contradicted the paradigm originating in the initial interpretation of the Halley Multicolour Camera data (e.g. Keller et al., 1987) which concluded that there were active and less active regions on the nucleus.

The shape influences the gas coma in two ways. On the one hand, the surface features cause different illumination conditions and therefore different gas production rates if one assumes a homogeneous composition and outgassing as a simple function of insolation. Secondly, the topography itself causes structures in the gas distribution as has been demonstrated by, for example, (Keller et al., 1994) where crater-like features “collimated” the outflow.

In this paper, we compare the measured gas distribution in the near nucleus coma of Comet Tempel 1 (Feaga et al., 2007) with

\* Corresponding author. Fax: +41 31 631 4405.

E-mail address: [susanne.finklenburg@space.unibe.ch](mailto:susanne.finklenburg@space.unibe.ch) (S. Finklenburg).

simulated gas distributions generated using the Direct Simulation Monte Carlo (DSMC) method. These distributions have been generated in full 3-D using the shape model of Tempel 1 (Thomas et al., 2007). Firstly, we assume homogeneous surface properties, meaning that the sublimation rate is proportional to the Hertz–Knudsen flux at each surface element. In this way, we compare the observed gas distribution with a model which follows the Crifo hypothesis (Crifo et al., 2002) of outgassing proportional to local insolation. In a second model, we adopt an activity distribution suggested by Kossacki and Szutowicz (2008). We will call this “the KS model”. These authors used the activity of Tempel 1 over its orbit derived from ground-based observations and concluded that the data would be best matched if only certain areas were active. They calculated the production rate with the so-called “long tube” formula and suggested different thicknesses of the dust crust to explain the different production rates. The long tube formula consists of the Hertz–Knudsen flux scaled with a dust layer dependent constant. It is therefore in principle similar to the proportionality factor,  $C$ , used in the homogeneous model and the icy area fraction used by Crifo (1997). The only difference is, that we use here the values suggested by Kossacki and Szutowicz who found them by fitting the observed production rates over whole orbits from Comet 9P/Tempel 1 to their model. Thirdly, we tested an ad hoc model modified from the KS model which was an attempt to fit  $H_2O$  column densities as measured by Feaga et al. (2007). This will be called the “Estimated model”. Finally we show results of a variation of the Estimated model, where the production rate is the same as before, but the surface temperature is everywhere constant at 200 K. This was done to show the impact of the surface temperature on the column densities and the radiation map.

In the next section, we shall discuss some of the inputs needed. Then the DSMC method and the specific implementation that we use will be described. We will also explain why DSMC is required here (rather than use of a fluid approach) and how the high density regions can be treated. In Sections 2.1–2.3 we explain the three different boundary conditions (models) which were simulated. The results are shown in Section 3 and we draw our conclusions in Section 4.

### 1.2. Source values, inputs, and constraints

The total production rate of Comet 9P/Tempel 1 at the time of the Deep Impact fly-by (2005–07–04) was estimated to be  $5 \times 10^{27}$   $H_2O$  molecule/s (Schleicher, 2007),  $9.4 \pm 0.69 \times 10^{27}$   $H_2O$  molecule/s (DiSanti et al., 2007) and  $4.6 \times 10^{27}$   $H_2O$  molecule/s (Feaga et al., 2007) using independent methods. The total surface area is approximately 120  $km^2$  which is an output of the shape model produced by Thomas et al. (2007) using the Deep Impact camera measurements. The smallest facet of the shape model has a size of 100  $m^2$ ; the largest one is 10,000  $m^2$ ; the average facet size is around 4000  $m^2$ . The surface temperatures are between 272 K and 336 K on the sunlit hemisphere (Groussin et al., 2007a, 2007b). Groussin et al.’s temperature map has a resolution of about 120 m.

The effusion velocity of a gas which leaves the surface with a half-Maxwellian is given by  $v_{eff} = \sqrt{\frac{2kT}{\pi m}}$ . Note that, as we consider here only a half-Maxwellian and not a full one, there is a mean velocity greater than zero. The half-Maxwellian is directed in a way, that all molecules leaving the surface have a velocity component pointing away from the surface. We assume this velocity distribution function (VDF) in the three models. With an approximate temperature of 300 K and a molecular mass of  $3 \times 10^{-26}$  kg for  $H_2O$ ,  $v_{eff} \sim 300$  m/s. If we assume that only half of the nucleus is active, the local production rate would be between  $8 \times 10^{19}$  and  $1.6 \times 10^{20}$  molecules/ $m^2/s$  for homogeneous dayside emission depending on the surface temperature. With the estimated

effusion velocity, the number density,  $n$ , at the surface is then between  $3 \times 10^{17}$  and  $5 \times 10^{17}$  molecules/ $m^3$ . Note that we used here the expression for a half-Maxwellian above the surface and neglect all backscattered molecules. The mean free path of a water molecule in the VHS (variable hard sphere; Bird, 1994) model is  $\lambda = \left(\sqrt{2}\pi d_{ref}^2\right)^{-1} \left(\frac{T}{T_{ref}}\right)^{\omega-0.5} \frac{1}{n}$ . For the VHS parameters of water, we use  $d_{ref} = 6.15 \times 10^{-10}$  m,  $T_{ref} = 300$  K, and  $\omega = 1.1$  (Crifo, 1989).  $\omega$  is the temperature exponent in the viscosity power law. This results in mean free paths above the sunlit surface of 1.2–2.4 m. Note that we have used for this estimation the simpler VHS model instead of the VSS model which we use later. The parameters are chosen in a way that the results of the two models are similar. On the night side, as well as further away from the surface, the mean free paths are greater (up to more than 5 km on the night-side) because of the lower densities. If the gas production is more localised on smaller areas, the local densities can be higher and the mean free path therefore smaller.

The Deep Impact observations of the water distribution in the vicinity of the nucleus provide the principal constraint on our model. It should be noted that we use two aspects of the results in Feaga et al. (2007). Firstly, the image of the water distribution in the immediate vicinity of the nucleus is used (Feaga et al., 2007; Fig. 11, second line in this paper; Fig. 5 in Feaga et al., 2007) for qualitative comparison. In order to be able to compare Feaga’s observations, which is a radiance map, with our simulation result, which is a density, several computational steps and assumptions have to be made. First we integrate our densities over the line of sight of the observation conditions. This gives the column density maps which will be shown later. Then we assume that the water band at the comet is optically thin. It is not immediately obvious that this is sufficient because estimations by Feaga et al. (2007) show that the strongest water line is most probably optically thick close to the nucleus. However, the observed water band comprises many lines so that the total emission comes from lines which are mostly optically thin. Furthermore, our model predicts higher rotational temperatures than assumed by Feaga et al. which should reduce the optical thickness. With this assumption, our radiance maps (Figs. 7, 9 and 11) give upper limits. We will argue below that the assumption of low optical thickness is probably sufficient.

Clearly, Feaga et al.’s radiance map constrains the source distribution and the position of putative active regions. However, we also use the determination of water column densities at 7 km resp. 3.8 km distance from the nucleus which are given numerically in the Feaga et al. paper as a quantitative constraint.

We seek to test various hypotheses against these constraints using 3D-DSMC modelling.

### 1.3. DSMC

The DSMC method was described by Bird (1994). The basic idea is that large numbers of real gas molecules are represented by a smaller number of simulation molecules. These simulation molecules move and collide with each other in a statistical way. All molecules within one collision cell at the time of the collision step can collide with each other. The collision pairs are chosen randomly. The macroscopic gas properties such as density, velocity and temperature are calculated by averaging the appropriate quantity over all simulation molecules in a sampling cell. The detailed formulae are found for example in Bird (1994). The rotational temperature is calculated by giving each simulation molecule an “internal temperature” and energy is redistributed partially between the internal and external degrees of freedom in each collision (Larsen–Borgnakke model (Borgnakke and Larsen, 1975)). The efficiency of this redistribution is parameterized by the rotational relaxation collision number which is given by the

Parker model (Parker, 1959). The molecular collisions are calculated with the variable soft sphere (VSS) scheme (Koura and Matsumoto, 1991). The model parameters were found by fitting the viscosity and the self-diffusivity description of the VSS model to the results from an extended corresponding states principle analysis (Xiang, 2001) of water. The details are described in Finklenburg (2014). The temperature exponent is 0.923. The VSS parameter is 0.929 and the reference diameter at a reference temperature of 300 K is 5.072 Å.

It is clear that the separation of the microscopic behaviour of a gas in a translational step and a collision step as required by DSMC is only valid if the mean distance between two colliding molecules is smaller than the mean free path. With separation, we mean that the movement and collision of simulated particles in the DSMC simulation are uncoupled such that particles first move and then collide with each other based on an instantaneous collisional probability. The ratio of the mean collisional distance (the mean distance between two colliding simulation molecules in the simulation) to the mean free path has to be smaller than 1. Bird (1994) proposed a value of 0.3 as an appropriate limit. This constrains the size of the collision cells (the cells in which the collisions are calculated).

The DSMC program used in this paper is PDSC<sup>++</sup> (Su, 2013) which is based on the PDSC code under development by Wu's group since 2000 (Wu and Lian, 2003; Wu and Tseng, 2005). The PDSC<sup>++</sup> code allows a parallel simulation of 2D and 3D flows on unstructured grids. The unstructured grid is defined with the help of the software GRIDGEN<sup>™</sup> before the DSMC simulation is started. The parallel performance is optimised by the use of a domain re-decomposition method.

The domain re-decomposition method includes four steps: (1) The initial DSMC simulation to reach a steady state using very few particles (e.g., ~one particle per cell) based on the domain decomposition with approximately an equal number of cells in each domain; (2) re-decompose the domain based on the particle number distribution obtained in Step (1); (3) decrease the particle weighting to increase the total number of particles for a better statistical accuracy (e.g., lower statistical uncertainties), and (4) perform the final DSMC simulation. We have found that for most DSMC simulations which look for steady-state solutions, this approach is very powerful and simple. For the study presented here, the approach is appropriate.

In addition, this version of PDSC<sup>++</sup> can employ hybrid grids in two- and three-dimensional cases including either triangles, quadrilaterals or mixed for the former, and either tetrahedrons, pyramids, prisms, hexahedrons or mixed for the latter.

The main difference between DSMC and fluid dynamics methods such as Navier–Stokes or Euler Equations solvers is that DSMC does not have any constraints on the degree to which the gas might be in a non-equilibrium state. Over every outgassing surface there is a non-equilibrium layer called the Knudsen layer. In the 2D case (evaporation from an infinite, flat surface), it takes about 200 mean free paths to reach 99% of the equilibrium value (Cercignani, 2000). Cercignani approximates the velocity distribution function of the gas in the Knudsen layer by a combination of a drifting Maxwellian and two semi-Maxwellians, one pointing towards the surface and one away from it. We speak here from “reaching 99% of the equilibrium value” when the contribution from the drifting Maxwellian to the total velocity distribution function is 99%.

The case of evaporation from a sphere was studied by Lukianov and Khanlarov (2000). They characterize the flows by their global Knudsen number which is the ratio of the mean free path to the radius of the source. In our case, the “global” radius of Tempel 1 is about 3 km. With a mean free path of the order of meters, the global Knudsen number is of the order of  $10^{-3}$ . Locally the curvature can be greater and therefore this estimate is a lower limit.

Lukianov and Khanlarov (2000) found that, for global Knudsen numbers larger than  $10^{-3}$ , the non-equilibrium boundary layer (Knudsen layer) goes over into a zone where there is non-equilibrium because of the expansion. Their criterion to define local thermal equilibrium is that the difference between the temperatures has to be less than 5%. (They use either the “temperatures” measured in radial and normal direction or the difference between translational and rotational temperature to determine non-equilibrium.)

We conclude that while there may be regions in the flow field where CFD (computational fluid dynamics) methods could be used, these regions are in fact small. The exact size and shape of these regions depends on the CFD method used. The Euler equations assume local thermal equilibrium everywhere while the Navier–Stokes equations allow small deviations. Also the degree of accuracy one wants to have influences the regions suitable for CFD methods. It is also difficult to couple the two solution methods and to define suitable boundary conditions for the fluid approach although this was done by e.g. Burt and Boyd (2009), Schwartzentruber and Boyd (2006), Wu et al. (2006) and others. There are Knudsen layer correction factors (e.g. Cercignani (1980) for polyatomic gas) but the thickness is unclear and depends on the local production rate (as explained above, the Knudsen layer thickness is a function of the mean free path of the gas and this depends on the density and therefore on the production rate). Typically one assumes local thermal equilibrium at the sonic surface, the surface at which the Mach number becomes 1. This is the largest thickness for which one can calculate the Knudsen layer with the approach suggested by Cercignani (1980) and Ytrehus (1975). Local thermal equilibrium has to be assumed there in order to have well defined input conditions for the CFD part. The shape of this surface, which is typically used as a starting surface in CFD solvers, is only in special cases similar to the shape model (Crifo et al., 2003, Fig. 4). Given these difficulties we have chosen to use an alternative method for optimising the DSMC method for simulation of higher density gas flows.

#### 1.4. Variable time-step (VTS) scheme

This procedure is basically the same as the one proposed by Kannenberg and Boyd (Kannenberg and Boyd, 2000; Kannenberg, 1998). If the cell size is set to be proportional to the local mean free path, then it is inversely proportional to the number density,  $n$ , for the three-dimensional case. The volume of such a cell in three dimensions is therefore proportional to  $n^{-3}$ . As the number of particles per cell is proportional to the cell volume times the number density, in this idealised case it is proportional to  $n^{-2}$ . Low density regions therefore have more particles than needed for a good DSMC simulation. This will lead to great computational waste, especially in regions far away from the comet and above the night side. To avoid this problem, a variable time-step (VTS) scheme (Wu et al., 2004) has been proposed to obtain a more uniform spatial distribution of simulated particles. The basic idea of the VTS scheme is to enforce the conservation (mass, momentum and energy) of moving simulated particles when crossing the interface between two neighbouring cells. If neither the number of particles nor their velocity should change this implies that the ratio of a weighting factor to the local time step has to be constant over the whole simulation region. As the number density is a priori unknown one assumes again that the cell size is proportional to the mean free path and therefore to  $n^{-1}$ . One assumes therefore that the number density is proportional to  $\frac{1}{\sqrt[3]{V}}$ , where  $V$  is the cell volume. The cell size is thereby assumed to be proportional to the local mean free path, even though it is not strictly true everywhere in the computational domain. One has to remember that the grid is constructed before the simulation run and it is

therefore up to of the user to build a mesh with cells of a volume that depends on the local mean free path (which is unknown and requires estimating). The local weighting factor,  $W_i$ , should be inversely proportional to the local number density in order to have a uniform distribution of simulation particles. Therefore the local weighting factors are set to be  $W_i = W_{\min} \sqrt[3]{\frac{V_i}{V_{\min}}}$ . The timestep,  $\Delta t$  is then found by the condition that the ratio  $\frac{W_i}{\Delta t_i} = \frac{W_{\min}}{\Delta t_{\min}}$  and therefore  $\Delta t_i = \Delta t_{\min} \sqrt[3]{\frac{V_i}{V_{\min}}}$ . One of the advantages in implementing the VTS scheme is to reduce both the number of simulated particles and the number of transient time steps to reach steady state, at which point the simulation particle property sampling normally starts in DSMC. This will result in appreciable time saving for the steady DSMC simulation. The VTS scheme does not ensure the same physical time everywhere in the computational domain. Thus, it can only be used for obtaining the steady-state solution, which most DSMC simulations do. However, it is highly efficient in reducing the total number of particles and number of steps towards the steady state.

In this paper, the VTS scheme is used for all simulations.

### 1.5. Transient adaptive sub-cell (TAS) method

As stated above, to have reliable results with the DSMC method, the distance between two colliding molecules (the mean collisional spacing, mcs) should be smaller than the mean free path (mfp) of the gas. In standard DSMC procedures, the two colliding molecules are chosen randomly from a cell. Their position inside the cell is ignored. This means that the cell size has to be small compared to the mean free path in order to fulfil the requirement. This leads, especially in a 3-D flow field, to an enormous number of cells. In our case, this would be more than needed for the required resolution. A further minor issue is that the result files become large which makes them hard to handle. The way around these issues is to use “transient adaptive subcells” or TAS (Su et al., 2010).

The TAS method is similar to Bird’s subcell method employed on a structured grid, in which the number of subcells depends on the ratio of local mean free path to the local cell size. This has been further extended to the case of unstructured grids (Su et al., 2010). To the best knowledge of the authors, Ivanov’s group has not used this idea to improve the collision quality; instead, this group used their own so-called Majorant Collision Frequency Scheme (Venkatraman et al., 2012) to improve the collision quality. TAS divides every collision cell dynamically into many subcells based on the number of simulation particles and the collision partners are chosen to be in the same or in adjacent subcells. There are on average 2 simulation particles per subcell. This allows one to find nearest neighbours for the collisional step and reduces thereby the mcs. Note that the subcells are only used to find the nearest neighbours. The result files still have the coarser resolution of the sampling cells.

There might be some concern because normally many more than two simulation particles per cell are required. This requirement is correct for the sampling cells, but we are talking here about the sub-cells. In PDSC++, we dynamically divide the sampling cell (or background cell) into different numbers of subcells based on local conditions in the sampling cell (number of particles). We divide the sampling cell into many sub-cells. We select randomly the first particle from the particles in the cell and then select the second by searching through the particles in the same subcell. If not, then neighbouring subcells are searched for the second particle until it is found. In this way, we can guarantee the almost near-distance 2nd particle can be selected. Fig. 1 shows a typical 2D example. The number of sub-cells in each coordinate direction is estimated as  $\sqrt{N_{\text{cell}}/P}$ . Here,  $N_{\text{cell}}$  and  $P$  is the number of particles

per background cell and the number of particles per sub-cell. Based on our experience, 2 particles per subcell are enough to guarantee a good quality of collision, even though the cell size is much larger than the local mean free path. Indeed, there are many more than 2 particles in the background cell in general. For more details one can refer to Su et al. (2010).

In these simulations, it turns out that the mcs/mfp ratio is, even with the transient adaptive subcells, larger than 1 in some regions. We tested the influence of this problem for our case by running one simulation with a coarser grid and without TAS (1,119,719 cells and max. 7,000,000 particles) and then the same case with a finer grid and TAS (6,191,856 cells and max. 10,000,000 particles). Note that “max.” gives the maximum number of particles which can be calculated. This number is not equal to the number of particles used in the simulation. The only information given about the real number of simulation particles is that this is smaller than this maximum number. By doing this we wanted to test the two extremes. Above the region with the highest production rate on the dayside, the mcs/mfp is about 40 in the TAS case and more than 100 in the coarser grid case. The largest difference in the column densities in the orientation we use for comparison with Deep Impact observations is about 8%. This is in a small region on the night side where both simulations have mcs/mfp values of less than 0.1. Therefore, the dominant differences occur in the rarefied regions which should not be caused by the grid. We suspect that the large differences in the rarefied regions are caused by numerical scattering together with the fact, that the density in this region is very low so that small absolute differences produce high relative errors. The mean difference over the whole flow field is about 2% which therefore provides an estimate of the numerical error caused by the high mcs/mfp ratio. Therefore we conclude that the presented results allow us to compare with the measured data to an accuracy which is probably better than 10%. For the presented models, the fine grid with TAS was used throughout.

It should be noted that use of TAS does not have a major impact on computational speed (computation times are around 5% longer using TAS) which is also a significant advantage given the long computation times necessary for 3D rarefied gas dynamics calculations.

## 2. The simulated models

For all models, we used the 3D shape model from Thomas et al. (2007). The coordinate system is defined in Thomas et al. (2007). The coordinate origin is at the centre of mass of the model assuming a homogeneous internal mass distribution. The spin vector, which defines the north–south axis, is along the calculated maximum moment of inertia. Finally, the prime meridian is set at the centre of a 350 m crater. SPICE (Acton, 1997) gives the sub-solar point as the interception point between the comet surface and the comet–Sun line at the time 2005-07-04T05:39:18 to be 12.6°W (=347.4°E) and 13.7° latitude. This is the time of observation 9000039 which was used for the high resolution temperature map (Groussin et al., 2007a, 2007b). This is used as the position of the sub-solar point in our modelling. The vector describing the viewing direction for the Feaga et al. observations is [0.358, −0.830, −0.427] in our cometocentric coordinate system.

The simulations were typically run with a maximum of  $10^7$  particles in around  $6 \times 10^6$  cells. The smallest timestep was  $1 \times 10^{-3}$  s.  $3 \times 10^4$  timesteps were simulated. Unfortunately, there is no strict criterion by which we could decide if steady state was reached. Beside the fact that 30 s is more time than needed by the average molecule to reach the end of the simulation region, we checked if the total number of simulation molecules was still changing with time. As there no systematic increase of this number in the last seconds was visible, we concluded that a steady state

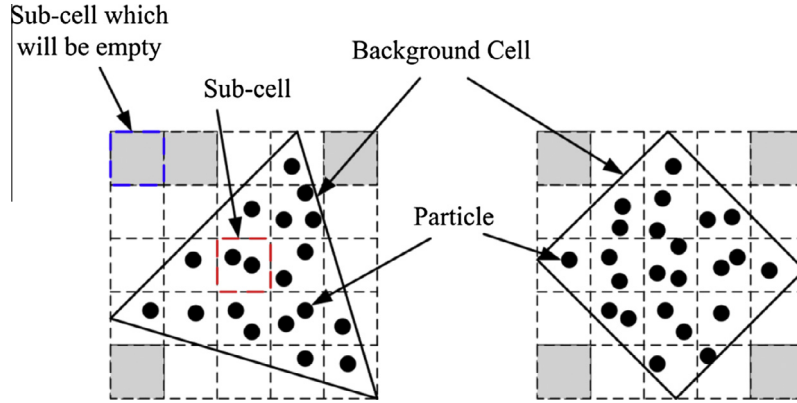


Fig. 1. Schematic showing the division of a 2D unstructured background cell into sub-cells using the TAS method: (left) triangular and (right) quadrilateral cell.

was reached. We used TAS as well as VTS to optimise the computation. Given that each simulation run requires 12 h of computation on a 32 CPU parallel system, it should be clear that a comprehensive investigation of the possible parameter space is not computationally feasible and hence some “guesswork” has been used with respect to the source distributions to limit the number of runs while still retaining consistency with the constraints. Besides the computation time, it should be noted that a surface distribution of sources of unknown extent cannot be described by a single parameter which can be varied to cover all possibilities. Therefore each case has to be developed by hand. This excludes an automatic parameter study.

### 2.1. Homogeneous surface model

In the homogeneous model, we assume that the gas flux is everywhere proportional to the Hertz–Knudsen flux, i.e.

$$Q(T) = C \sqrt{\frac{m}{2\pi kT}} p_{\text{sat}}(T) \text{ (kg/m}^2 \text{ s)} \quad (1)$$

$$p_{\text{sat}}(T) = i_1 e^{-\frac{i_2}{T}} \text{ (Pa)} \quad (2)$$

With  $i_1 = (3.23 + 0.73/-0.38) \times 10^{12}$  Pa and  $i_2 = 6134.6 \pm 17.0$  K (Gundlach et al., 2011).  $Q$  is the local water vapour flux,  $m$  is the mass of a water molecule,  $k$  is the Boltzmann constant,  $T$  is the local temperature of the sublimating surface,  $p_{\text{sat}}$  is the local saturation vapour pressure at the given temperature and  $C$  is a proportionality constant smaller than 1.  $C$  is determined by the total production rate which is set to  $9.4 \times 10^{27}$  molecules/s (DiSanti et al., 2007) in this model.

The temperature is the equilibrium temperature under the assumption that the thermal conductivity into the interior is negligible and only IR emission and the net sublimation play a role, i.e.

$$\frac{S_c}{R_h^2} (1 - A_b) \max(\cos(\alpha), 0) = \sigma \epsilon T^4 + Q(T)H \quad (3)$$

$$H = \frac{k}{m} i_2 \text{ (J/kg)} \quad (4)$$

Here,  $S_c = 1360$  W/m<sup>2</sup> is the solar constant,  $R_h = 1.51$  AU is the heliocentric distance of the comet at the time of the encounter,  $A_b = 0.014$  is the visible Bond albedo (Groussin et al., 2007a, 2007b),  $\alpha$  is the solar zenith angle,  $\sigma = 5.6704 \times 10^{-8}$  W m<sup>2</sup> K<sup>4</sup> Stefan–Boltzmann constant,  $\epsilon = 0.9$  for consistency with Groussin et al. (2007a, 2007b) and  $H(T)$  is the enthalpy of sublimation (Gundlach et al., 2011).

The shape model is quite smooth so that there are no obvious regions where shadow could play a role other than on the regions

which face away from the Sun and they are included in Eq. (3). Also, there is no diffusion from the interior considered.

To calculate the model we used the solar zenith angles given by the SPICE system (Acton, 1997). For each surface element, its centre was used as a reference point for which the solar zenith angle and the temperature was calculated. This value was then assumed to be the same for the whole element. The resulting boundary conditions are shown in Fig. 2a (Temperature) and Fig. 2b (Production rate). The temperatures are between 6 K and 316 K (measurements: “272–336 K on the sunlit hemisphere”; Groussin et al., 2007a, 2007b). The minimum temperature has been set artificially to be consistent with no gas production. There is simply no gas production on the night side. The maximum temperature (316 K) arises because in matching the desired production rate, the proportionality constant,  $C$ , becomes less than 1, and the requirement for energy balance, implicit in Eq. (3), forces the temperature to this value.

Simulation molecules returning to the surface are absorbed.

### 2.2. The KS model

Here we simulate a nucleus with a dust layer height distribution as suggested by Kossacki and Szutowicz (2008). We refer to this as the “KS model” and the paper from which it is derived as “KS”.

The temperature map was calculated by neglecting all heat transfer into the interior and assuming that all incoming energy is emitted. The emissivity,  $\epsilon$ , was calculated such that the equilibrium temperature at the sub-solar point, which was the hottest region on the nucleus, is 336 K – the maximum measured (Groussin et al., 2007a, 2007b). This gives an emissivity of 0.82. On the night side the minimum temperature was arbitrarily set to 80 K. KS do not discuss the nightside temperature, but as most of it is covered by a thick dust layer in our model, the exact value of the nightside temperature does not play a big role. Even if it would be much higher, the 2 m thick dust layer (see below) would, on the one hand, not conduct enough heat to the subsurface and, on the other hand, the gas could hardly diffuse through it in the relevant time scales.

The relevant equation is

$$\frac{S_c}{R_h^2} (1 - A_b) \max(\cos(\alpha), 0) = \sigma \epsilon T^4 \quad (5)$$

Fig. 3 compares our temperature model with the one published by Groussin et al. (2007a, 2007b). In order to facilitate the comparison, the temperature scales are the same. Note again that

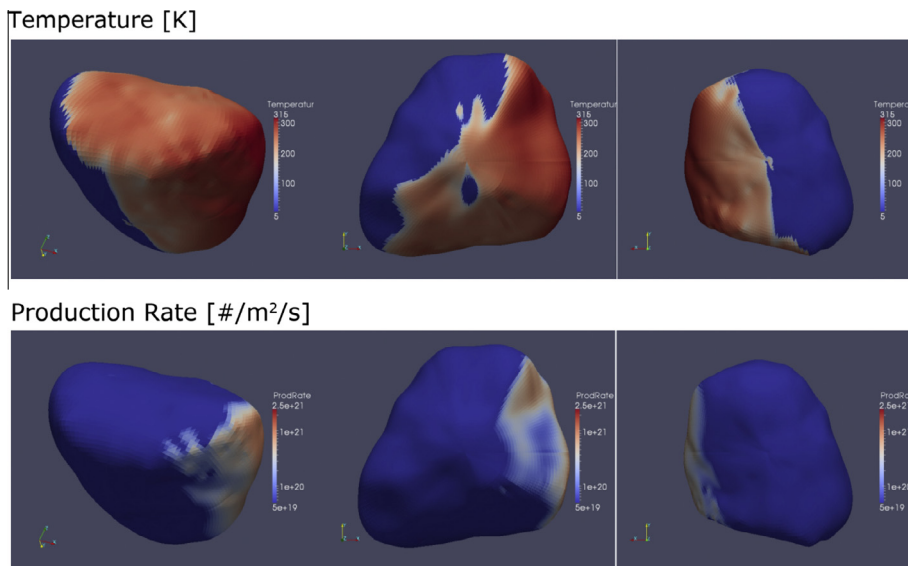


**Fig. 2.** Top row: Surface temperature in the “homogeneous surface” case. In the first picture, the Sun is to the right and the shown axes give the orientation of the cometocentric coordinate system as defined in “tempel1\_coordinates.lbl”. The z-axis is the rotation axis and the x-axis points toward the prime median. This orientation is the one in which the observations at the time 2005-07-04T05:39:18 UTC were made. The second and the third picture show the view on the rotation poles of the comet. Second row: Production rate in molecules/m<sup>2</sup>/s in the “homogeneous surface” model. The orientation of the images is the same as in the first row.

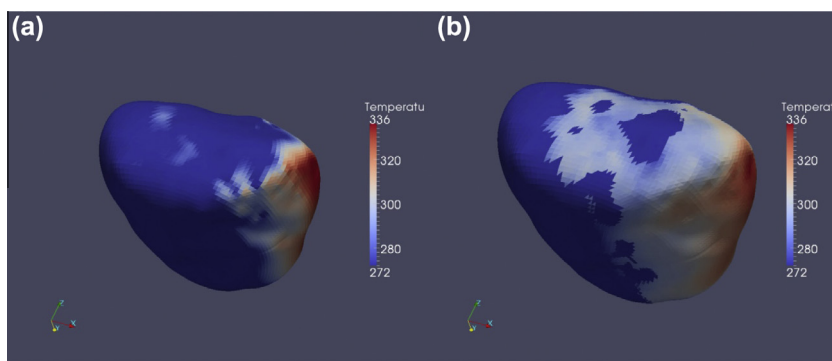


**Fig. 3.** (a) Temperature distribution in the KS model. The minimum temperature is 80 K. The emissivity is 0.82 – a value set by the condition that the maximum temperature should be 336 K at the sub-solar point. The albedo is 0.014 (Groussin et al. (2007a, 2007b)). Tempel 1 was at a heliocentric distance of 1.51 AU. (b) Temperature map of Groussin et al. (2007a, 2007b). The dark blue regions are the ones without measurements or where no temperature data were given. (For interpretation of the references to colour in this figure legend, the reader is referred to the web version of this article.)

the lowest temperature in the model has been set to 80 K (on the night side where there are no observations) and not 272 K which was the lowest measured temperature.

The temperature of the subliming layer just below the surface is calculated by the condition that all energy conducted to the interior goes into sublimation. The thermal conductivity of the surface is constant and assumed to be  $\kappa = 2 \times 10^{-2}$  W/m/K, as given in KS for a non-uniform dust mantle.

KS describe the flow coming through a dust layer thicker than 0.5 cm with the long tube formula:

$$Q(T) = \frac{8}{3} \frac{r_d \Psi_d}{\tau \Delta_d} \sqrt{\frac{m}{2\pi kT}} p_{\text{sat}}(T) \quad (\text{kg/m}^2 \text{ s}) \quad (6)$$

with  $r_d$  is the effective pore radius (0.10 mm),  $\Psi_d$  is the porosity of the dust layer (0.73),  $\tau$  is the tortuosity (assigned a value of  $\sqrt{2}$ ) and  $\Delta_d$  is the thickness of the dust layer (KS). With,  $r_d$ ,  $\Psi_d$ , and  $\tau$  held constant, the production rate is a function of the assumed temperature and the dust layer thickness. As input for our simulation, only the gas density inside an imaginary subsurface reservoir and its temperature are needed as input conditions. To speculate about

the physical processes which could produce these conditions is out of the scope of this paper.

In the KS paper, the nucleus is represented by an ellipsoid and is divided into 32 sectors. According to their analysis, only 3 of these 32 sectors should be active. KS use 4 longitude sectors, 90° apart with the first sector starting at 0°. There are 8 latitude sectors with centres at  $\pm 61^\circ$ ,  $\pm 30^\circ$ ,  $\pm 21^\circ$  and  $\pm 12^\circ$ . The 3 active sectors “are centred at the latitudes  $-12^\circ$ ,  $-21^\circ$  and  $-30^\circ$  at any longitudes among four that are analysed in the model with the 32 sectors. In the selected 3 sectors, the dust layer is only 1 cm thick, while the remaining surface is covered by a thick isolating mantle.” As KS use the equatorial bulge as zero longitude the longitude values are shifted by about 40° with respect to the grid defined by Thomas et al. (2007).

We have chosen the longitudes from those proposed by KS in a way to fit the observed gas distribution best because we have no rotational phase constraints. Also it is clear in KS’s paper that low activity at high latitudes does not change the total production rate significantly at any position along the orbit. Such an activity is observed by Feaga et al. (2007) but is not present in the KS analysis. Therefore in the KS model presented here we have added a small

source at high latitude, called the north polar source in the following, to attempt agreement without breaching the observational constraints.

The active sectors and their location as well as their dust layer thicknesses are given in Table 1. Sectors 2, 3, 4 are the ones described by KS. All other sectors (numbers 1, 5 and 6) were added to fit the observed gas distribution. Note that sector 6, the north polar source, is smaller than a single cell and a smoothing function has been applied. The parameters inside each surface element are constant. The smoothing makes the boundary between the different sectors less sharp by changing the dust layer thickness over about 5 surface elements. The resulting dust thickness distribution is shown in Fig. 4.

Outside the sectors listed in Table 1, the dust layer is 2 m thick and the surface therefore practically inactive. The heights of the dust layer at the sides of the sectors were smoothed to minimise structures appearing because of jumps in the boundary conditions at sector boundaries. The gas density directly above the surface also depends on the local temperature. Therefore the density maps are not simply proportional to the dust layer thickness. The density map can be seen in Fig. 5.

In total 32.5% of the total surface is “active” and produces 96% of the total gas flux. The total amount of gas produced is  $7.65 \times 10^{27}$  H<sub>2</sub>O molecule/s. This is in the middle of the range of gas production rates found by various authors (see above and Table 4). Note that we deliberately used here the long-tube formula and the best fit values from the KS paper to compare the results from this paper as directly as possible with Feaga et al.’s results.

Simulation molecules hitting the surface are absorbed.

### 2.3. Estimated model and its constant temperature variant

A case was calculated in which the dust layer thickness was chosen “by hand” in a way to reproduce the observed gas distribution to a higher degree of fidelity. Only water vapour was simulated. In this case, we focused on reproducing the lower limits of the column densities at 3.8 km and 7 km distance given in Feaga et al. (2007).

The distribution of the sectors on the nucleus in this “Estimated” model is similar to the KS model. But sector 6 was changed and some sectors are essentially “inactive” because their dust layer thickness is the same (0.4 m) as the one of the “inactive” regions. The returning molecules are treated in the same way as before. The difference is that the dust layer thicknesses have been changed and the temperature model is different. The position of the sectors and the dust layer thicknesses are given in Table 2.

The temperature was taken from Groussin et al. (2007a, 2007b) (Fig. 3b). Everywhere where there was no temperature measurement, the minimum measured (272 K) was assumed. This gives much higher night side temperatures than the modelled

temperature maps used in the KS model. However, the long-tube formula we are using here has two parameters (the surface temperature and dust layer thickness) to control the production rate. Hence, the outgassing rate is controlled by a dust layer of varying thickness. In the Estimated model, the maximum thickness assumed is  $L = L_{\max} = 0.4$  m so that, together with the higher night-side temperatures, emission from the nightside is non-negligible. Fig. 6 shows the resulting initial number densities and the local production rates.

The total production rate is here  $4 \times 10^{27}$  molecules/s and therefore slightly below the observed production rates.

Finally, we simulated a situation in which the production rate is everywhere the same as in the Estimated model. Therefore also the total production rate is the same. The difference is, that in this variation, the initial temperature of the gas is everywhere constant at a value of 200 K. By comparing the Estimated model with its variant one can therefore estimate the importance of the initial temperature to the column densities and the radiation maps.

## 3. Results

Feaga et al. (2007) measured the distribution of water vapour, CO<sub>2</sub> and dust in the vicinity of the nucleus using the High Resolution Instrument Infrared Spectrometer (HRI-IR). In their paper, two observations are of immediate interest to us.

Firstly, radiance maps of the spectral lines of the different gases are shown. We concentrate here on the water vapour which is assumed to be the dominant gas component and not influenced by flows of other species. The water vapour radiance map from Feaga et al. (2007) is shown in Fig. 11 (second line) to provide comparison with our best model. Assuming that the vapour is not optically thick, the radiance is proportional to the column density along the line of sight. We assume an optically thin atmosphere and calculate the radiance resulting from a given number density with the formula (Feaga et al., 2007):

$$\text{Radiance} = \frac{N g h c}{r^2} \frac{1}{\lambda 4\pi}$$

with  $N$  being the number density in particles per square metre and  $g = 2.85 \times 10^{-4} \text{ s}^{-1}$  being the  $g$ -factor of water at 1 AU.  $r = 1.51$  AU is the heliocentric distance at the time of the observation,  $h$  is the Planck constant,  $c$  is the speed of light,  $\lambda = 2.66 \times 10^{-6} \text{ m}$  is the central wavelength of the emission band. The radiance is then given in ( $\text{W}/\text{m}^2/\text{sr}$ ).

Secondly, Feaga et al. gave lower limits on the column density at 3.8 km resp. 7 km distance from the centre of the nucleus. These are listed in Table 3.

In order to compare the simulation results with Feaga’s et al. results we need to compute column densities. When computing the column density, we must account for the finite size of the simulation region. Simply adding up the densities leads to artefacts at the edges. The problem is, that when the simulation region is a sphere and you add up all cells which lie behind each other in the line of sight, then there are more cells in the lines going through the centre of the sphere and only very few cells on the sides. In the extreme case, on the edges, there is only a single cell. In order to avoid these artefacts, a radial  $r^{-2}$  dependence of the gas density is assumed outside of the simulated 10 km sphere so that a simple integration of the column can be made. The densities along the line of sight are summed up and then displayed in a colour plot. The radiance is calculated from these column densities to be compared directly with Fig. 11.

In addition, the column densities at 3.8 km resp. 7 km distance from the centre of the nucleus have been calculated to be compared with the lower limits measured by Feaga et al. (2007).

**Table 1**

Boundary conditions for the KS model.  $L$  is the thickness of the dust layer in the active regions and it is  $L = 10^{-2}$  m thick. The dust layer of the inactive regions is 2 m thick.

Sector nr.	Mid latitude <sup>a</sup> (min; max)	Mid longitude (min; max)	Thickness of dust layer
1	−61° (−90°; −45.5°)	0° (0°; 360°)	2L
2	−30° (−45.5°; −25.5°)	85° (40°; 130°)	L
3	−21° (−25.5°; −16.2°)	0° (315°; 45°)	L
4	−12° (−16.2°; 0°)	0° (315°; 45°)	L
5	(45.5°; 70°)	270° (225°; 315°)	L
6	(89°; 90°)	0° (0°; 360°)	10L

We assumed that the boundary between two adjacent sectors was in the middle: e.g. for −30° and −21° the boundary should be at  $(-30^\circ + 21^\circ)/2 = 25.5^\circ$ .

<sup>a</sup> The given value for the mid-latitudes is the one given in Kossacki and Sztowicz (2008).

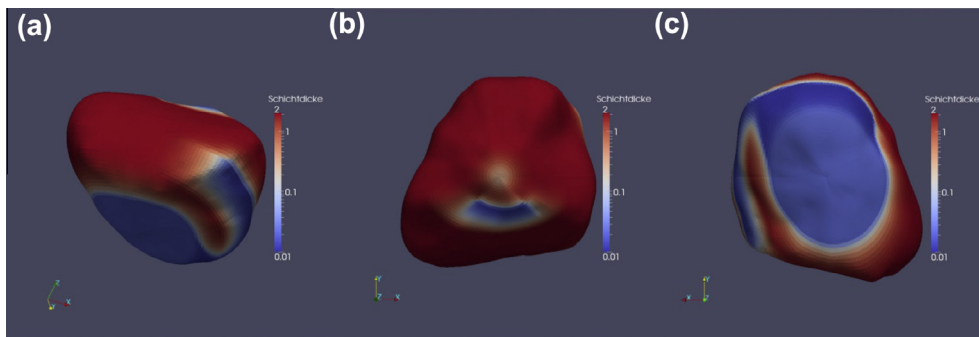


**Fig. 4.** The dust layer thickness of the KS model seen from different perspectives. (a) Observation perspective, (b) North pole, and (c) South pole.

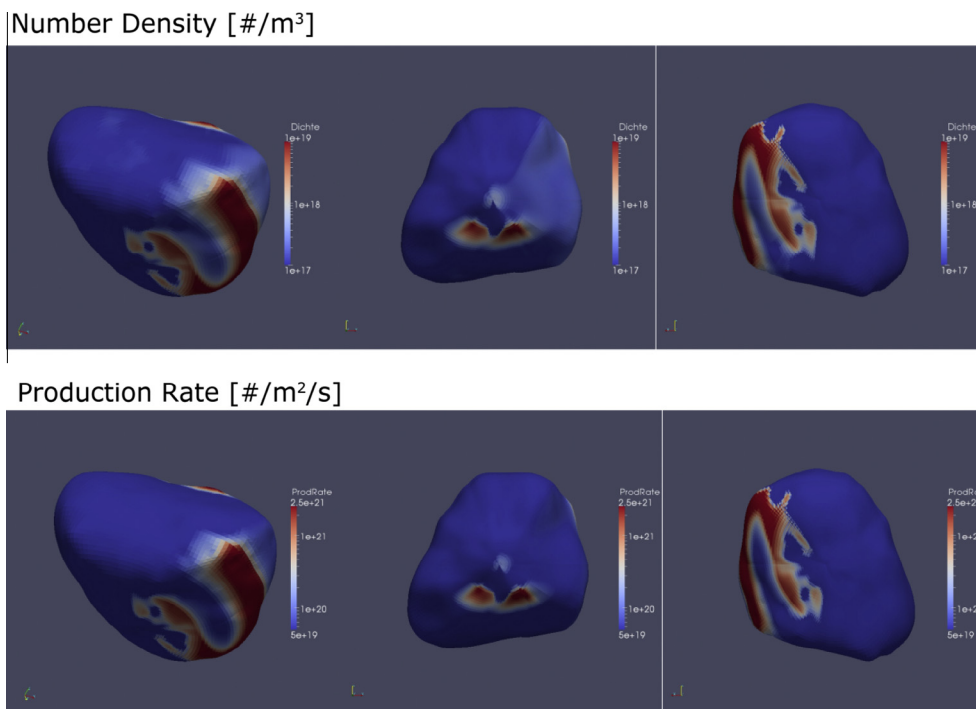


**Fig. 5.** First row: Initial number density of the KS model shown from different perspectives. Left: Observation perspective, middle: North pole, right: South pole. The scale is logarithmic and goes from  $1 \times 10^{17}$  to  $1 \times 10^{19}$  particles per  $m^3$ . Second row: Production rate of the KS model. The orientation is the same as in the first row. The scale is logarithmic and goes from  $5 \times 10^{19}$  to  $2.5 \times 10^{21}$  particles per  $m^2$  per second.

**Table 2**

Boundary conditions for the Estimated model.  $L = 0.4$  m dust layer thickness. The dust layer thickness of the inactive areas is also 0.4 m and therefore much smaller than in the KS model. Note that the sectors 2, 3, 5 and 6 are not different from the inactive area any more.

Sector nr.	Mid latitude (min; max)	Mid longitude (min; max)	Thickness of dust layer
1	$-61^\circ$ ( $-90^\circ$ ; $-45.5^\circ$ )	$0^\circ$ ( $0^\circ$ ; $360^\circ$ )	$1.5L$
2	$-30^\circ$ ( $-45.5^\circ$ ; $-25.5^\circ$ )	$85^\circ$ ( $40^\circ$ ; $130^\circ$ )	$L$
3	$-21^\circ$ ( $-25.5^\circ$ ; $-16.2^\circ$ )	$0^\circ$ ( $315^\circ$ ; $45^\circ$ )	$L$
4	$-12^\circ$ ( $-16.2^\circ$ ; $0^\circ$ )	$0^\circ$ ( $315^\circ$ ; $45^\circ$ )	$0.1L$
5	( $45.5^\circ$ ; $70^\circ$ )	$270^\circ$ ( $225^\circ$ ; $315^\circ$ )	$L$
6	( $70^\circ$ ; $90^\circ$ )	$0^\circ$ ( $0^\circ$ ; $360^\circ$ )	$L$

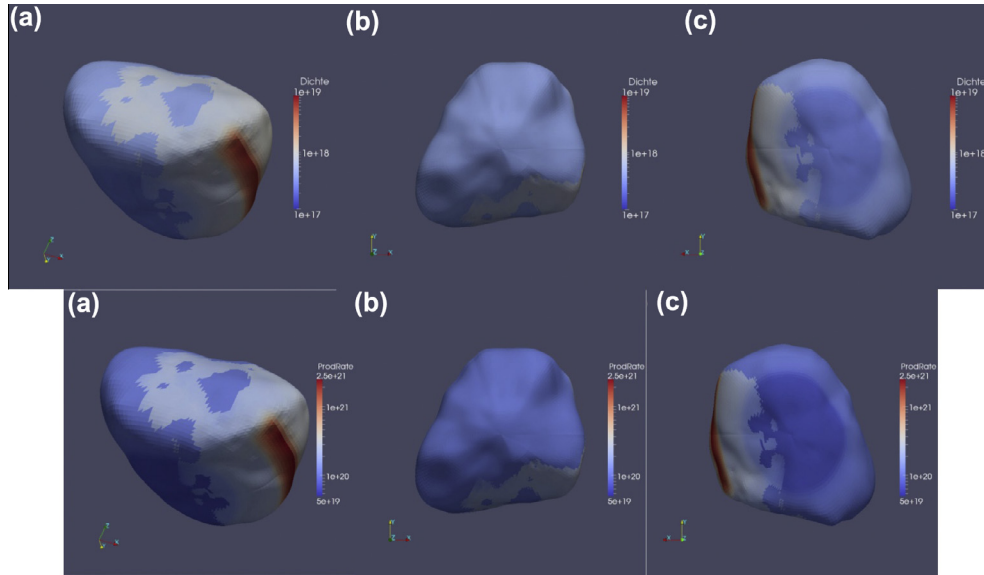
Finally, the simulated production rates are compared to the observations (Table 4).

Fig. 7 shows the column densities in the case of the homogeneous model. There is only one region with high density and this is close to the subsolar point. There is little emission from the poles which is contrary to the measurements. Fig. 8 compares the

measured column densities at 3.8 km and 7 km distance to the nucleus with the ones given as lower limits by Feaga et al. (2007). It is obvious that this model fails to match either the near-nucleus radiance map or the column density limits at 3.8 km and 7 km. It can be immediately concluded that an outgassing from a homogeneous surface with a half-Maxwellian emission from each facet of the given shape model is not compatible with observations.

Figs. 9 and 10 show the column density map, the radiance map and the column densities at 3.8 km and 7 km distance for the KS model. In this model, there is more emission in the direction of the poles and the column density map shows a number of similarities with the observations. Specifically, the highest column densities are well represented in the model. The peak of the water column density in the model is no longer above the sub-solar point but accurately representing the more southerly activity. The added north polar source fits the observation reasonably well although a south polar source might be additionally needed. On the basis of the column density map alone one might conclude that the KS model (with slight modification) is actually a good fit to the data. However, there are significant differences in the column densities





**Fig. 6.** First row: Initial number density in molecule/m<sup>3</sup> for the Estimated model. The colour scale is logarithmic and the same as in the figure for the KS model ( $10^{17}$  molecules/m<sup>3</sup> in dark blue to  $10^{19}$  molecules/m<sup>3</sup> in red). Second line: Production rates in molecules per square meter per second for the Estimated model. The colour scale is logarithmic and goes from  $5 \times 10^{19}$  molecules/m<sup>2</sup>/s (dark blue) to  $2.5 \times 10^{21}$  molecules/m<sup>2</sup>/s (red). (a) Observation perspective, (b) North pole, and (c) South pole. (For interpretation of the references to colour in this figure legend, the reader is referred to the web version of this article.)

**Table 3**

Table 3 from Feaga et al. (2007) giving the lower limits for the water column densities in 7 km distance from the centre of the nucleus together with the estimated position of the region. The angle to the x-axis is in the projected view as Fig. 11, second line. The angles are not given by Feaga et al. but simply estimated from the figures.

Region	H <sub>2</sub> O (molecules m <sup>-2</sup> )	Distance from the centre of the nucleus (km)	Angle to x-axis (°)
Ecliptic north	$>6.9 \times 10^{20}$	~3.8	60–135
Positive rot. pole	$>2.8 \times 10^{20}$	~7	15–60
Sunward	$>4.0 \times 10^{20}$	~7	0–15; 315–360
Ecliptic south	$>7.1 \times 10^{20}$	~3.8	240–315
Negative rot. pole	$>2.9 \times 10^{20}$	~7	195–240
Anti-sunward	$>2.0 \times 10^{20}$	~7	135–195

**Table 4**

Overview of the different production rate measurements and calculations at the time of the Deep Impact encounter.

	Total production rate estimate (molecules/s)
Feaga et al.	$4.6 \times 10^{27}$
Schleicher	$5 \times 10^{27}$
DiSanti et al.	$9.40 \pm 0.69 \times 10^{27}$
Homogeneous model	$9.4 \times 10^{27}$
KS model	$7.65 \times 10^{27}$
Estimated model	$4 \times 10^{27}$

at 3.8 km and 7 km. The North pole and night side emission are below the lower limits set by Feaga et al. and the angular position of emission peaks do not fit.

Figs. 11, 12 and 14 show the results of the Estimated model and Fig. 11 (second line) shows Feaga et al.'s radiance map for comparison. Here, the column density map does show the high density region south of the subsolar point and the fit is generally rather good. There are two points where the simulated radiation map differs significantly from the observed one. On the one hand, there is a region close to the surface on the nightside where limited emission was observed. Further out from this point, the observed radiation is

higher again. In our simulation, we find a higher radiation close by the surface and a steady decrease going outwards. The lack of radiation close to the nucleus may be caused by shadowing effects or inhomogeneous nightside emission not accounted for in the model. On the other hand, there is the south polar region (below the nucleus in Fig. 11). Here our simulation shows less radiation than Feaga et al.'s observations. In the KS model simulations (Fig. 9) we find more radiation in this region, but even more than observed. We conclude therefore, that both proposed models are not ideal in this region. A better model will have an intermediate production rate in this region. The column density at 3.8 km and 7 km distance from the centre of the nucleus (Fig. 14) is now much more similar to the measured values and everywhere close to or above the lower limit. Also the total production rate of  $4 \times 10^{27}$  molecules per second is within 15% of the measured production rate.

We conclude that this model is superior to the other two models of outgassing. It should be clear however that we have selected sources and source strengths in a somewhat ad hoc manner and that there is improvement possible. The problem is almost certainly severely under-constrained and the solution we present is undoubtedly not unique. On the other hand, we can, at this point, show the properties of the flow should this particular solution be valid.

One alternative solution is the variation with the constant initial temperature shown in Fig. 13. In the column density map, the difference between the Estimated model and its variant is barely visible. In the radiance map, which is simply proportional to the column density, the differences are clearer but still small. Due to the lower initial temperature, the gas expands slower and the density is slightly higher. The gas velocity 10 km from the centre of the source is in this case, about 700 m/s compared to the 900 m/s in the Estimated model. But the main features of the column density and radiation maps are very similar in both Estimated models although the initial temperature distribution varies significantly.

Fig. 15 shows the speed of the gas along a line along the vector [1, 0, 0] (in cometocentric coordinates). Because we used an unstructured grid, it is highly unlikely to have points exactly on this vector. We show therefore the points in the vicinity of this

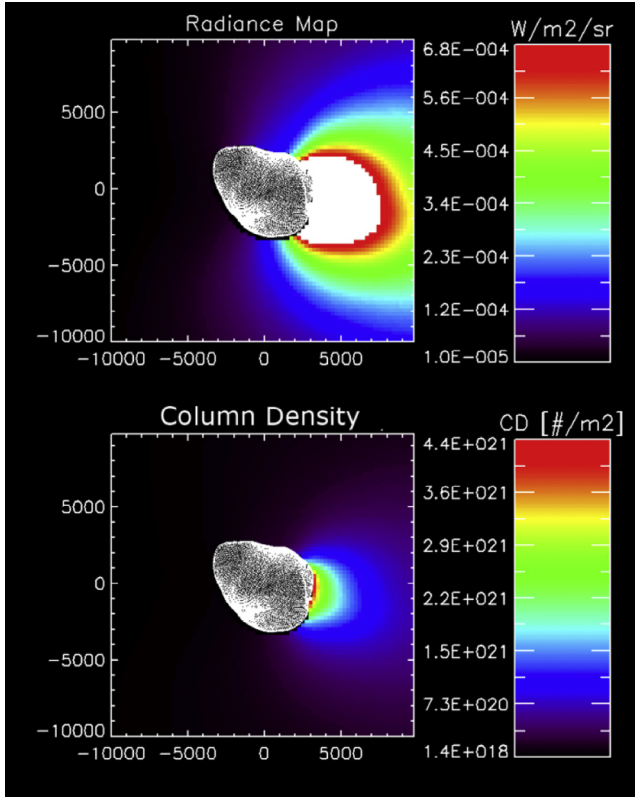


**Fig. 7.** Column densities in the case of the homogeneous model. The numbers on the axes are the distances from the centre of the nucleus in meters.

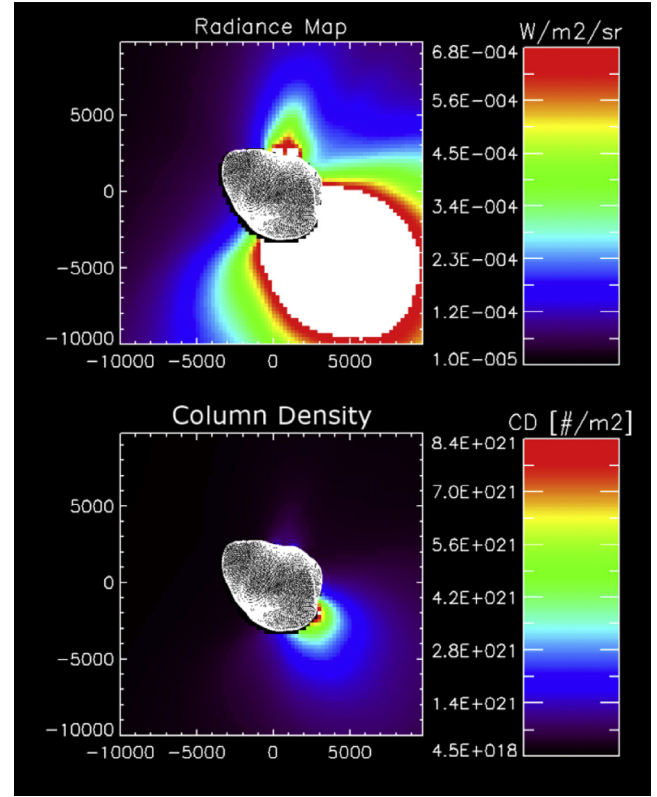


**Fig. 9.** Column densities in the case of the KS model. The orientation is again with the Sun to the right and the ecliptic North pole to the top. The numbers on the axes are the distances from the centre of the nucleus in meters.

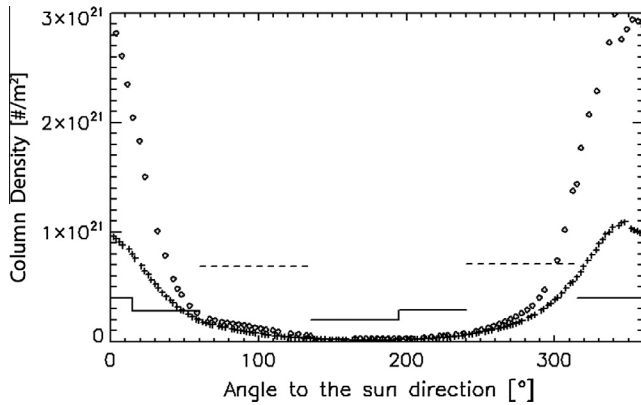


**Fig. 8.** Column densities at 3.8 km and 7 km distance from the centre of the nucleus in the case of the homogeneous model (given in molecules per  $m^2$ ). The simulation results are shown as crosses (7 km) or diamonds (3.8 km); the solid line represents the column densities estimated by Feaga et al. (2007) for 7 km distance, the dashed lines are Feaga et al.'s data for 3.8 km distance.

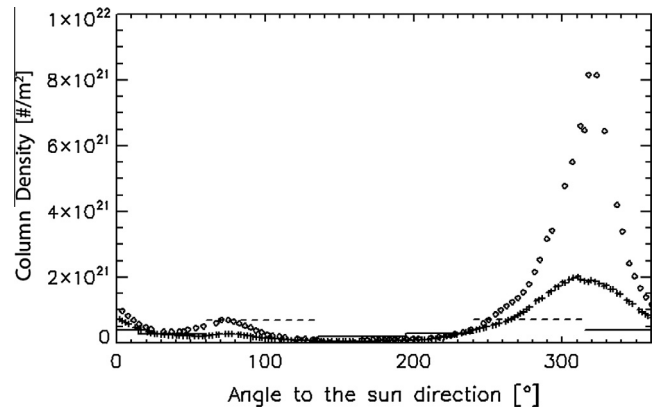


**Fig. 10.** Column densities at 3.8 km and 7 km distance to the nucleus for the KS model (given in molecules per  $m^2$ ). The crosses represent the simulation results, the solid lines are Feaga et al.'s (2007) estimated column densities for the 7 km distance from the source. The diamonds and the dashed lines show the simulated values resp. the Feaga et al. (2007) estimates for the 3.8 km distance case.

vector. (We calculate the scalar product of the position vector of the centre point of each cell scaled to have norm 1 and the direction vector which is also scaled to have norm 1. If this product is larger than 0.999, the point is considered to be along the given vector.)

It is obvious that the gas does not reach its final velocity in the simulated 10 km domain. Also this final velocity will be clearly more than the 500 m/s assumed in the Feaga et al. (2007) paper to calculate production rates. We note that Gombosi et al. (1986) using a fluid approach also found higher gas velocities than the 500 m/s assumed. We note that the column densities used by Feaga et al. to calculate the total production rate vary by a factor of two within their two “bins”. Therefore there is some imprecision

in the given value. Comparing our velocities to values found by other groups and for other cases does not seem to be useful as the velocity depends on the initial gas temperature and this varies for the different thermophysical nucleus models and the different heliocentric distances for which the various models were calculated.

One can try to estimate the final gas velocity by approximating the comet by a sphere. Then the gas flow field is given by the formulas in Sone and Sugimoto (1993). For the free molecular (collisionless) flow approximation, the final velocity is simply  $u_{\infty,c} = 2\sqrt{\frac{2kT_0}{\pi m}}$  which is about  $u_{\infty,c} = 34.3\sqrt{T_0}$  in (m/s) for water

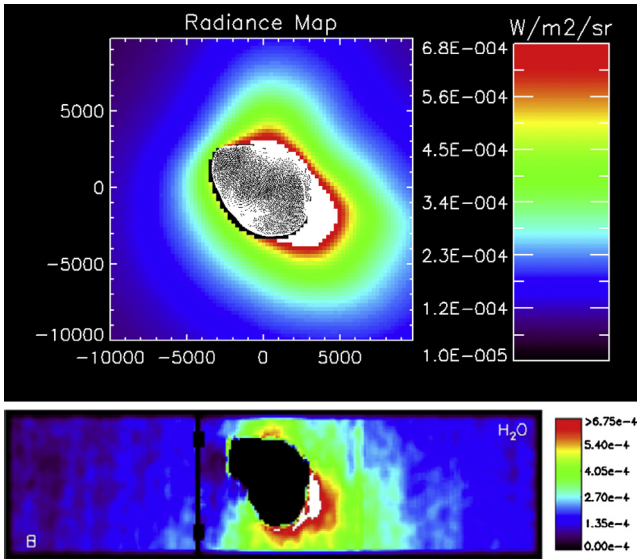


**Fig. 11.** Top: Estimated model, radiance map ( $\text{W m}^{-2} \text{sr}^{-1}$ ). The Sun is to the right and the ecliptic north to the top. The comet nucleus is marked with white dots, the black squared underneath it, are the regions without data. The distances are given in meters. Bottom: Radiance map from Fig. 5 in Feaga et al. (2007). The colour bar indicates the radiance values ( $\text{W m}^{-2} \text{sr}^{-1}$ ) along the line of sight. The field of view is  $43 \text{ km} \times 10 \text{ km}$ . The Sun is to the right. (For interpretation of the references to colour in this figure legend, the reader is referred to the web version of this article.)

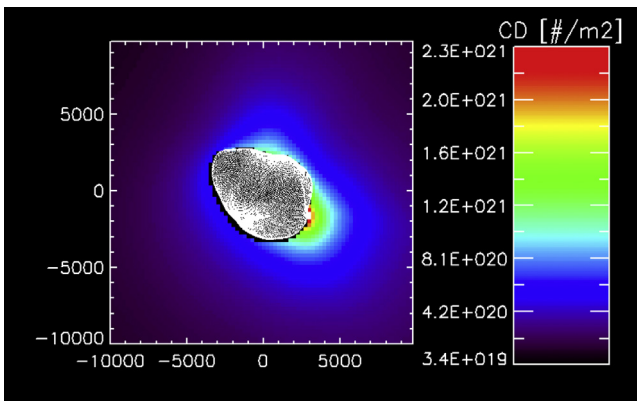


**Fig. 12.** Estimated model, column densities ( $\text{m}^{-2}$ ). The Sun is to the right and the ecliptic north to the top. The comet nucleus is marked with white dots, the black squared underneath it, are the regions without data. The distances are given in meters.

vapour.  $T_0$  is the initial gas temperature (K),  $k$  the Boltzmann constant and  $m$  the mass of a single molecule in (kg).

In the fluid limit and for three internal degrees of freedom, the formulae given in Sone and Sugimoto (1993) have to be slightly changed (see for example, Finklenburg, 2014). They give the formulae for gases with no internal degrees of freedom. In the fluid limit, the Mach number of the flow goes to infinity at an infinite distance from the source. For this case, one finds that  $u_{\infty f} = \sqrt{\frac{28kT_s}{3m}}$ .  $T_s$  is here the temperature at the sonic surface (K). As we look at the fluid limit, we neglect the Knudsen layer thickness and assume that the Knudsen layer can be described by its 1D model described in Cercignani (2000). For a gas with 3 internal degrees of freedom,  $\frac{T_s}{T_0} = 0.814$  and one finds for water that  $u_{\infty f} = 59.2\sqrt{T_0}$  m/s.

In the Estimated model, the initial gas temperature in the region close to the  $[1, 0, 0]$  vector is about 320 K. Therefore the final

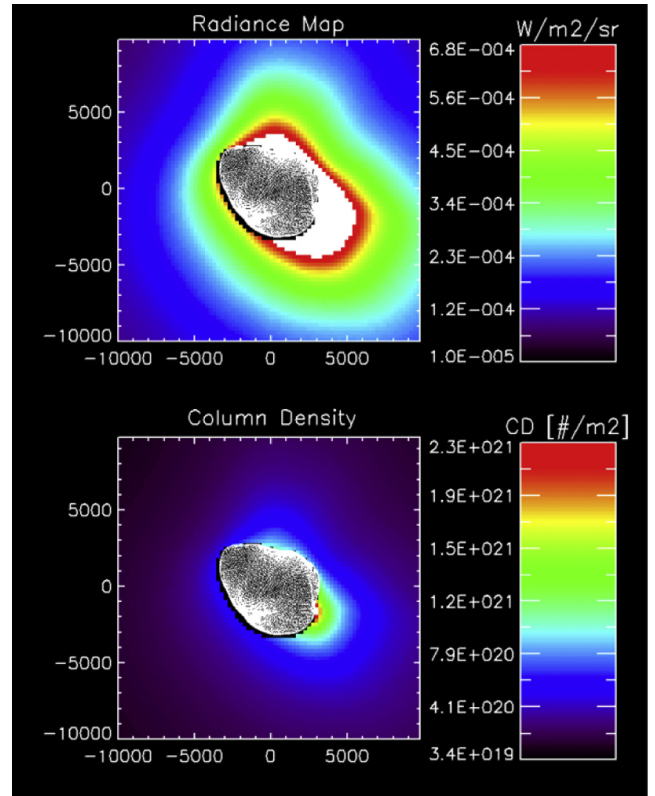


**Fig. 13.** Estimated model with constant surface temperature of 200 K. The radiance map and the column densities are given with the same scales as used for the Estimated model in Figs. 11 and 12. Due to the lower initial temperature, the gas densities are slightly higher as can be best observed in the radiance map.

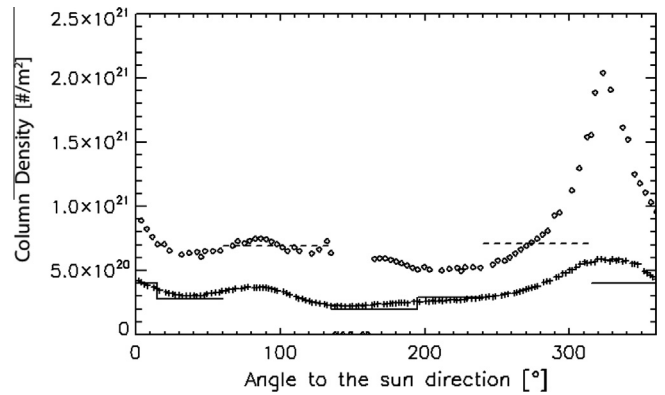


**Fig. 14.** The column densities at 3.8 km and 7 km distance from the centre of the nucleus for the Estimated model (given in molecules per  $\text{m}^2$ ). The simulation results are marked with crosses (7 km) or diamonds (3.8 km), the lower limits from Feaga et al. (2007) are shown as solid line (7 km) or dashed line (3.8 km).

velocities are  $u_{\infty f} = 614 \text{ m/s}$  and  $u_{\infty f} = 1059 \text{ m/s}$ . The velocity at the end of the simulation region at this position is about 900 m/s but there is clearly still an acceleration going on.

In the 200 K surface temperature variant of the Estimated model, the initial gas temperature is 200 K and one finds the values  $u_{\infty f} = 485 \text{ m/s}$  and  $u_{\infty f} = 837 \text{ m/s}$ . At the end of the simulation region, the velocity is at about 700 m/s and again there is still an acceleration noticeable.

We note also that the pure fluid description is probably not correct as the gas rarefies with expansion. Therefore values below the fluid estimation are expected. The simulation results are therefore consistent with expectation.

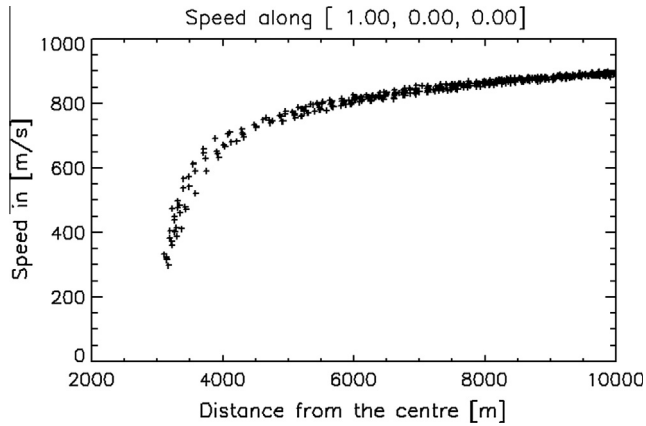


Fig. 15. Speed of the gas along the model x-axis. The speed is given in m/s. The data are for the Estimated case.

Fig. 16 shows different gas parameters in cuts through the origin of the cometocentric coordinate system. The local number density is the first parameter shown in Fig. 16. The second row shows the mean free path of the gas. It is nearly everywhere larger than 1 m but, inside the simulation region, smaller than 100 m. That means that it is everywhere large compared to dust grains but small compared to the cometary size. This, in turn, implies that a free molecular aerodynamic approach in modelling the dust flow would be acceptable (e.g. Bird, 1994).

The third parameter shown in Fig. 16 supports this result. It shows the degree of non-equilibrium by presenting the ratio of the rotational temperature to the translational one. This value is everywhere close to, but larger than 1. That it is larger than 1 is expected because there are no mechanisms to cool the rotational degrees of freedom other than collisions. The translational temperature drops because of the expansion. Therefore the rotational degrees of freedom are always warmer or equal in energy with respect to the translational ones. That the simulation result is everywhere close to one, indicates that the gas is close to a local thermal equilibrium.

The total temperature is shown in the last row of Fig. 16.

Fig. 17 shows the speed and the gas velocities in the radial direction and perpendicular to it as well as the ratio of these two velocities. By comparing the plots, it is immediately clear that the radial flow is dominant outwards from about 1 nucleus radius above the surface. But there are perpendicular velocities which are not negligible. The flow field <1 nucleus radius from the surface is extremely complex. The perpendicular velocities are especially high close to the surface. This is the region where dust is mostly accelerated as the gas is densest there. Therefore a complex spatial distribution of dust might be expected.

Going back to Fig. 6, second row, one can compare the typical nightside to a typical dayside production rate of the Estimated model. Note that the colour bar is logarithmic. The highest dayside production rates are about  $2.5 \times 10^{21}$  molecules/m<sup>2</sup>/s. The nightside production rate is only around  $1 \times 10^{20}$  molecules/m<sup>2</sup>/s and hence considerably lower than the local dayside production but clearly non-negligible.

#### 4. Conclusions and discussion

Three different models (and one variant) of the outgassing of Comet 9P/Tempel 1 were simulated and compared with Deep Impact measurements. The measurements used were a radiance map in an H<sub>2</sub>O emission line, an estimation of a lower limit of the column densities at different points around the nucleus in the inner coma, and the total production rate.

It is clear that a nucleus, uniformly active in response to solar insolation, cannot explain the observed gas distribution around Tempel 1. Active regions are required which is in broad agreement with the conclusions of Farnham et al. (2012) and further supports the concept of inhomogeneous surface properties of cometary nuclei.

A model suggested by Kossacki and Szutowicz (2008) has also been studied. Their result appears to reproduce roughly the positions of active regions on the surface but with a number of limitations. The simulated near-nucleus radiance map is similar to the Deep Impact radiance map of Feaga et al. (2007) but the KS model requires additional polar sources to provide a better fit. However, the additional constraint provided by Feaga et al.'s numerical values for the column densities 3.8 km and 7 km from the centre of the nucleus is poorly reproduced by this model in particular because of the low nightside emission.

A modification of the KS model, the Estimated model, which uses a different temperature model and different dust layer thicknesses has been constructed to reproduce the column density at 3.8 km and 7 km distance from the nucleus. The approach was here rather successful in reproducing both the main features of the radiance map and the inferred column densities.

Finally a small variation of the Estimated model was also simulated. In this variation, the temperature on the surface is everywhere equal to 200 K. The column densities are slightly higher compared to the Estimated model, but the features and the distribution are not influenced significantly. We conclude that gas emission from the nightside of the nucleus is necessary to match the column densities given by Feaga et al. The calculations also show (e.g. in the KS model) that lateral flow (i.e. roughly parallel to the surface) of gas, which is a known and expected phenomenon (e.g. Keller and Thomas, 1989) and also present in our simulations, is not sufficient to populate the inner coma above the nightside to the required density. Raising the surface temperature to allow H<sub>2</sub>O outflow from the nightside surface in the model is required. The observations of Farnham et al. (2012) suggest that dust emission from the nightside does indeed occur and that emission may occur from regions which have been in darkness for at least 4 h. Hints of nightside activity have been seen previously in fly-by observations of other comets (e.g. Sagdeev et al., 1987). Here, in the absence of further constraints, we have used an approach which implies a hemispheric, homogeneous outgassing from the nightside. However, it should be clear that this approach does not offer a unique solution to the observed distribution.

The kinetic energy of the gas when it has its final velocity is, at the source, given in the form of a temperature. We have used here the surface temperature distribution of Groussin et al. (2007a, 2007b) to set this temperature as a constraint. As pointed out above, we are in essence assuming that the gas is emitted from an ice surface at approximately 200 K but immediately accommodates to the observed surface temperature as it flows through the surface layer before leaving the comet. The relationship between effusion velocity and initial temperature has been given above and would suggest a decrease in the outflow velocity of around 20% if the temperature of the gas exiting the surface is close to the free sublimation temperature of water ice.

As shown in Fig. 15, the velocity of the gas reaches almost 900 m/s at the edge of the simulation field. This is considerably higher than assumed by Feaga et al. (2007), for example, who consider 500 m/s in their analysis. The model also shows that lateral flows near the surface can locally reach 300 m/s with ratios of lateral to radial outflow velocity approaching 1 in some areas. This has immediate implications for simulations of the near nucleus region. For example, one cannot simulate only part of the surface unless the simulation encompasses all emission/activity. There are two main reasons. First, lateral flows entering the simulation

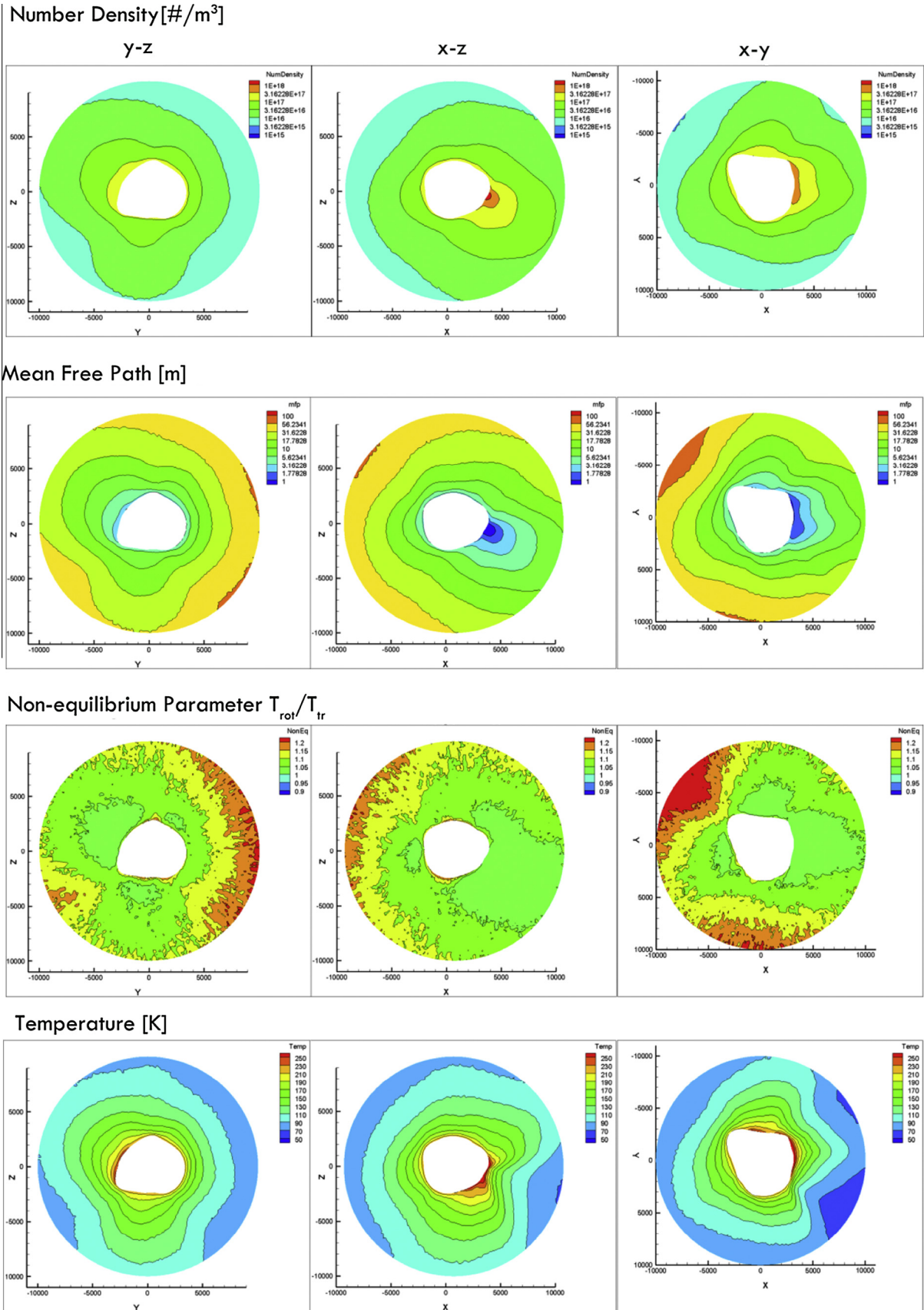


**Fig. 16.** Flow field parameters in cuts through the origin of the coordinate system. From left to right, one sees the yz-plane, the xz-plane and the xy-plane. Note that none of these plains is the observation plane, but the xz-plane comes closest to it. Top row: The number density: The colour bar is logarithmic and goes from  $10^{15}$  #/m<sup>3</sup> (dark blue) to  $10^{18}$  #/m<sup>3</sup> (red). 2nd row: The mean free path: The colour bar is logarithmic and goes from 1 m (dark blue) to 100 m (red). 3rd row: The non-equilibrium parameter ( $T_{rot}/T_{tr}$ ): The colour bar is linear and goes from 0.9 (dark blue) to 1.2 (red). Bottom row: The total temperature: The colour bar is linear and goes from 50 K (dark blue) to 250 K (red). (For interpretation of the references to colour in this figure legend, the reader is referred to the web version of this article.)

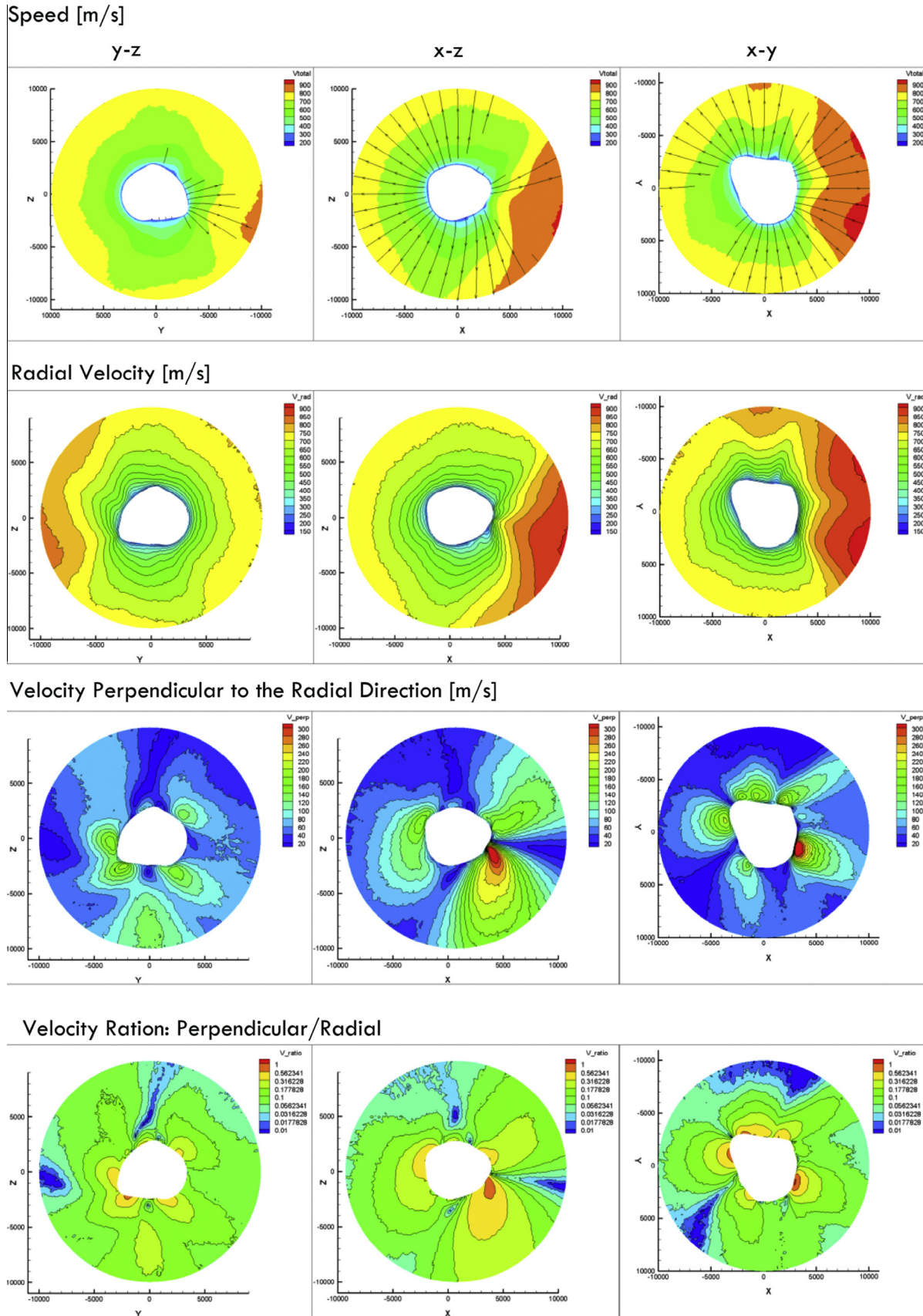


**Fig. 17.** Velocity components in cuts through the origin of the coordinate system. From left to right, one sees the yz-plane, the xz-plane and the xy-plane. Top row: Total speed in m/s and stream lines. The colour bar is linear and goes from 200 m/s (dark blue) to 900 m/s (red). Second row: Radial velocity: The colour bar is linear and goes from 150 m/s (dark blue) to 900 m/s (red). Third row: Velocity perpendicular to the radial direction: The colour bar is linear and goes from 20 m/s (dark blue) to 300 m/s (red). Bottom row: Velocity ratio: The colour bar is logarithmic and goes from 0.01 (dark blue) to 1 (red). (For interpretation of the references to colour in this figure legend, the reader is referred to the web version of this article.)

region, which are not modelled if one assumes vacuum or radial outflow at the boundaries of the flow field, can comprise significant energy in an active comet with the perpendicular to radial gas velocity ratio approaching one near the surface. Second, in good simulations, the velocities at outer boundaries should significantly exceed  $Ma = 1$  otherwise an artificial boundary layer of unknown thickness will form. When considering only a part of the surface, the boundary impinges upon the region directly above the surface with close to sonic flow. By using vacuum boundary conditions one effectively enforces supersonic flow at the boundary and removes particles which might continue to influence the flow. In our case, with a 10 km radius simulation region, the Mach number approaches 5 at the outer edge. In Fig. 15, there is no hint of a boundary layer which would be evident as an increased acceleration towards the outer boundary which suggests that our simulation region here is large enough to study the near-nucleus domain imaged by Deep Impact.

## Acknowledgments

This work has been supported by the Swiss National Science Foundation. We want to thank the referees for their helpful comments.

## References

- Acton, C.H., 1997. NASA's SPICE system models the Solar System. In: Wyrzyszczyk, I.M., Lieske, J.H., Feldman, R.A. (Eds.), *Dynamics and Astrometry of Natural and Artificial Celestial Bodies: Proceedings of IAU Colloquium*. Kluwer Academic Publishers, Poznan, p. 257.
- A'Hearn, M.F., Combi, M.R., 2007. Deep Impact at Comet Tempel 1. *Icarus* 191 (2), 1–3. <http://dx.doi.org/10.1016/j.icarus.2007.09.003>.
- Bird, G.A., 1994. *Molecular Gas Dynamics and the Direct Simulation of Gas Flows*. Oxford University Press.
- Borgnakke, C., Larsen, P.S., 1975. Statistical Collision Model for Monte Carlo Simulation of Polyatomic Gas Mixture.
- Burt, J., Boyd, I., 2009. A hybrid particle approach for continuum and rarefied flow simulation. *J. Comput. Phys.* 228 (2), 460–475. <http://dx.doi.org/10.1016/j.jcp.2008.09.022>.
- Cercignani, C., 1980. Strong evaporation of a polyatomic gas. In: *Rarefied Gas Dynamics*, 12th, pp. 305–320.
- Cercignani, C., 2000. *Rarefied Gas Dynamics*. Cambridge University Press.
- Crifo, J.F., 1989. Inferences concerning water vapour viscosity and mean free path at low temperatures. *Astron. Astrophys.* 223, 365–368.
- Crifo, J., 1997. The correct evaluation of the sublimation rate of dusty ices under solar illumination, and its implication on the properties of P/Halley nucleus. *Icarus* 130 (2), 549–551. <http://dx.doi.org/10.1006/icar.1997.5827>.
- Crifo, J.-F., Rodionov, A.V., Szegő, K., Fulle, M., 2002. Challenging a paradigm: Do we need active and inactive areas to account for near-nuclear jet activity? *Earth Moon Planets* 90, 227–238.
- Crifo, J.F., Loukianov, G.a., Rodionov, a.V., Zakharov, V.V., 2003. Navier–Stokes and direct Monte Carlo simulations of the circumnuclear coma II. Homogeneous, aspherical sources. *Icarus* 163 (2), 479–503. [http://dx.doi.org/10.1016/S0019-1035\(03\)00041-1](http://dx.doi.org/10.1016/S0019-1035(03)00041-1).
- DiSanti, M.a., Villanueva, G.L., Bonev, B.P., Magee-Sauer, K., Lyke, J.E., Mumma, M.J., 2007. Temporal evolution of parent volatiles and dust in Comet 9P/Tempel 1 resulting from the Deep Impact experiment. *Icarus* 187 (1), 240–252. <http://dx.doi.org/10.1016/j.icarus.2006.10.007>.
- Farnham, T.L., Bodewits, D., Li, J.-Y., Veverka, J., Thomas, P., Belton, M.J.S., 2012. Connections between the jet activity and surface features on Comet 9P/Tempel 1. *Icarus* 222 (2), 540–549. <http://dx.doi.org/10.1016/j.icarus.2012.06.019>.
- Feaga, L.M., A'Hearn, M.F., Sunshine, J.M., Groussin, O., Farnham, T.L., 2007. Asymmetries in the distribution of H<sub>2</sub>O and CO<sub>2</sub> in the inner coma of Comet 9P/Tempel 1 as observed by Deep Impact. *Icarus* 191 (2), 134–145. <http://dx.doi.org/10.1016/j.icarus.2007.04.038>.
- Finklenburg, S., 2014. *Investigations of the Near Nucleus Gas and Dust Coma of Comets*. Universität Bern.
- Gombosi, T.I., Nagy, a.F., Cravens, T.E., 1986. Dust and neutral gas modeling of the inner atmospheres of comets. *Rev. Geophys.* 24 (3), 667. <http://dx.doi.org/10.1029/RG024i003p00667>.
- Groussin, O., A'Hearn, M.F., Li, J.-Y., Thomas, P.C., Sunshine, J.M., Lisse, C.M., et al., 2007a. Surface temperature of the nucleus of Comet 9P/Tempel 1. *Icarus* 187 (1), 16–25. <http://dx.doi.org/10.1016/j.icarus.2006.08.030>.
- Groussin, Olivier, A'Hearn, M.F.M.F., Li, J.-Y., Thomas, P.C., Sunshine, J.M.J.M., Lisse, C.M., et al., 2007b. Surface temperature of the nucleus of Comet 9P/Tempel 1. *Icarus* 187 (1), 16–25. <http://dx.doi.org/10.1016/j.icarus.2006.08.030>.
- Gundlach, B., Skorov, Y.V., Blum, J., 2011. Outgassing of icy bodies in the Solar System – I. The sublimation of hexagonal water ice through dust layers. *Icarus* 213 (2), 710–719. <http://dx.doi.org/10.1016/j.icarus.2011.03.022>.
- Kannenberg, K.C., 1998. *Computational Methods for the Direct Simulation Monte Carlo Technique with Application to Plume Impingement*. Cornell University, Ithaca, NY.
- Kannenberg, K.C., Boyd, I.D., 2000. Strategies for efficient particle resolution in the Direct Simulation Monte Carlo method. *J. Comput. Phys.* 157 (2), 727–745. <http://dx.doi.org/10.1006/jcph.1999.6397>.
- Keller, H.U., Thomas, N., 1989. Evidence for near-surface breezes on Comet P/Halley. *Astron. Astrophys.* 226, L9–L12.
- Keller, H.U. et al., 1987. Comet P/Halley's nucleus and its activity. *Astron. Astrophys.* 187, 807–823.
- Keller, H.U., Knollenberg, J., Markiewicz, W., 1994. Collimation of cometary dust jets and filaments. *Planet. Space Sci.* 42 (5), 367–382.
- Kossacki, K., Szutowicz, S., 2008. Comet 9P/Tempel 1: Sublimation beneath the dust cover. *Icarus* 195 (2), 705–724. <http://dx.doi.org/10.1016/j.icarus.2007.12.014>.
- Koura, K., Matsumoto, H., 1991. Variable soft sphere molecular model for inverse-power-law or Lennard-Jones potential. *Phys. Fluids A* 3 (10), 2459–2465.
- Lukianov, G.A., Khanlarov, G.O., 2000. Stationary expansion of water vapours from the sphere surface into vacuum. *Thermophys. Aeromech.* 7 (4), 489–498.
- Parker, J.G., 1959. Rotational and vibrational relaxation in diatomic gases. *Phys. Fluids* 2 (4), 449–462.
- Sagdeev, R.Z. et al., 1987. The spatial distribution of dust jets seen during the Vega 2 flyby. *Astron. Astrophys.* 187, 835–838.
- Schleicher, D., 2007. Deep Impact's target Comet 9P/Tempel 1 at multiple apparitions: Seasonal and secular variations in gas and dust production. *Icarus* 190 (2), 406–422. <http://dx.doi.org/10.1016/j.icarus.2007.04.013>.
- Schwartzentruber, T.E., Boyd, I.D., 2006. A hybrid particle-continuum method applied to shock waves. *J. Comput. Phys.* 215, 402–416.
- Sone, Y., Sugimoto, H., 1993. Kinetic theory analysis of steady evaporating flows from a spherical condensed phase into vacuum. *Phys. Fluids* 5 (6), 1491–1511.
- Su, C.-C., 2013. *Parallel Direct Simulation Monte Carlo (DSMC) Methods for Modeling Rarefied Gas Dynamics*. National Chiao Tung University, Taiwan.
- Su, C.C. et al., 2010. Implementation of a transient adaptive sub-cell module for the parallel-DSMC code using unstructured grids. *Comput. Fluids* 39 (7), 1136–1145. <http://dx.doi.org/10.1016/j.compfluid.2010.02.003>.
- Sunshine, J.M. et al., 2006. Exposed water ice deposits on the surface of Comet 9P/Tempel 1. *Science (New York, NY)* 311 (5766), 1453–1455. <http://dx.doi.org/10.1126/science.1123632>.
- Thomas, P.C., Veverka, J., Belton, M.J.S., Hidy, A., A'Hearn, M.F., Farnham, T.L., et al., 2007. The shape, topography, and geology of Tempel 1 from Deep Impact observations. *Icarus* 187 (1), 4–15. <http://dx.doi.org/10.1016/j.icarus.2006.12.013>.
- Thomas, P., A'Hearn, M., Belton, M.J.S., Brownlee, D., Carcich, B., Hermalyn, B., et al., 2013. The nucleus of Comet 9P/Tempel 1: Shape and geology from two flybys. *Icarus* 222 (2), 453–466. <http://dx.doi.org/10.1016/j.icarus.2012.02.037>.
- Venkattraman, A., Alexeenko, A.A., Gallis, M.A., Ivanov, M.S., 2012. A comparative study of no-time-counter and majorant collision frequency numerical schemes in DSMC. In: *AIP Conference Proceedings*, pp. 489–495.
- Wu, J.-S., Lian, Y.-Y., 2003. Parallel three-dimensional Direct Simulation Monte Carlo method and its applications. *Comput. Fluids* 32 (8), 1133–1160. [http://dx.doi.org/10.1016/S0045-7930\(02\)00083-X](http://dx.doi.org/10.1016/S0045-7930(02)00083-X).
- Wu, J.-S., Tseng, K.-C., 2005. Parallel DSMC method using dynamic domain decomposition. *Int. J. Numer. Methods Eng.* 63 (1), 37–76. <http://dx.doi.org/10.1002/nme.1232>.
- Wu, Jong-Shinn, Tseng, K.-C., Wu, F.-Y., 2004. Parallel three-dimensional DSMC method using mesh refinement and variable time-step scheme. *Comput. Phys. Commun.* 162 (3), 166–187. <http://dx.doi.org/10.1016/j.cpc.2004.07.004>.
- Wu, J.-S., Lian, Y.-Y., Cheng, G., Koomullil, R.P., Tseng, K.-C., 2006. Development and verification of a coupled DSMC–NS scheme using unstructured mesh. *J. Comput. Phys.* 219 (2), 579–607. <http://dx.doi.org/10.1016/j.jcp.2006.04.013>.
- Xiang, H.W., 2001. The new simple extended corresponding-states principle: Complex molecular transport properties in dilute gas state. *Fluid Phase Equilib.* 187–188, 221–231. [http://dx.doi.org/10.1016/S0378-3812\(01\)00537-4](http://dx.doi.org/10.1016/S0378-3812(01)00537-4).
- Ytrehus, T., 1975. *Kinetic Theory Description and Experimental Results for Vapor Motion in Arbitrary Strong Evaporation*. <<http://repositorio.tudelft.nl/view/aereports/uuid:8421d890-9fd9-4736-93f3-eb2aa108e96c/>>.